Journal of Superconductivity and Novel Magnetism (2021) 34:2945–2955
https://doi.org/10.1007/s10948-021-06053-z

ORIGINAL PAPER

Transport Properties of Ce-Doped Cd Ferrites $CdFe_{2-x}Ce_xO_4$

Nasir Amin[1] · Abdul Razaq[1] · Atta Ur Rehman[1] · Khalid Hussain[1] · M. Ajaz Un Nabi[1] · N. A. Morley[2] · Mongi Amami[3,7] · Aisha Bibi[4] · Muhammad Imran Arshad[1] · Khalid Mahmood[1] · Muneeba Fatima[1] · Maria Akhtar[1] · Sofia Akbar[1] · Alina Manzoor[1] · Hafiz T. Ali[5] · Mohammad Yusuf[6] · Sana Amin[1]

Received: 10 April 2020 / Accepted: 8 September 2021 / Published online: 5 October 2021

Abstract

Cadmium ferrites belong to normal spinel ferrites, and they exhibit interesting electrical, magnetic, and optical properties. The pure and cerium-doped cadmium ferrites $CdFe_{2-x}Ce_xO_4$ ($x=0.0$, 0.125, 0.250, 0.375, 0.5) were synthesized by a chemical co-precipitating technique using sodium hydroxide as a co-precipitating agent. The structures and phase purity of fabricated nanomaterials were analyzed by X-ray diffraction (XRD). The crystallite size for all the prepared nanomaterials was in the range of 28–46 nm. The lattice constant and unit cell volume were found to decrease with the increasing concentration of Cerium, which was confirmed by the peak shift in the XRD pattern. The X-ray density for all nano ferrites increased with the enhancement of cerium composition. The resistivity of the nanomaterials has random behavior with the enhancement of cerium composition for a temperature, but the value of resistivity at $x=0.125$ has the lowest value and at $x=0.375$ has the highest value for almost all temperatures. For specific concentrations, a decreasing trend of resistivity of fabricated materials was found with an increment of temperature. The activation energies were also calculated, and it increased for $x=0.125$ and then decreased for all the nanomaterials. For the confirmation of the M–O bonds, FTIR analysis of all the nano ferrites was also performed. The analysis shows a higher frequency absorption band in the range of 531.24–534.84 cm^{-1}. This absorption band confirms that metal oxides are formed in all the synthesized nanoparticles.

Keywords Spinel · Ferrites · Absorption band · Resistivity · Activation energies

This article is part of the special issue "Selected articles based on 4th International Conference on *Materials Science & Nanotechnology*"

✉ Muhammad Imran Arshad
miarshadgcuf@gmail.com

1 Department of Physics, Government College University, Faisalabad 38000, Pakistan

2 Department of Materials Science and Engineering, The University of Sheffield, Sheffield S1 3JD, UK

3 Department of Chemistry College of Sciences, King Khalid University, P.O. Box 9004, Abha, Saudi Arabia

4 Institute of Functional Nano & Soft Materials (FUNSOM), Soochow University, Suzhou 215123, Jiangsu, China

5 Department of Mechanical Engineering, College of Engineering, Taif University, P.O. Box 1109, Taif 21944, Saudi Arabia

6 Department of Clinical Pharmacy, College of Pharmacy, Taif University, P.O. Box 1109, Taif 21944, Saudi Arabia

7 Laboratoire des Matériaux et de l'environnement pour le développement durable LR18ES10. 9 Avenue Dr. Zoheir SAFI, 1006 Tunis, Tunisia

1 Introduction

A hefty category of oxides are the ferrites which possess extraordinary magnetic characteristics. The researchers showed special interest in the investigation and application of these ferrites during the last 50 years. The applications of ferrites are included in the handling of power, electronic technology, and in the field of biotechnology. Spinel ferrites and natural spinel $MgAl_2O_4$ which was first found by Bragg possess identical crystal structures. Magnetite (Fe_3O_4) is an important ferrite, perhaps the oldest which has many applications. Research on ferrites is a very active research field nowadays. It has mesmerizing properties coupled close to the presence of F_e^{2+} and F_e^{3+} cations together. Soft ferrites have many applications in microwave devices, thermo-junctions, high-frequency cores, humidity sensors, antennas, multilayer chip indicators, high-frequency transformers, ferrite wave absorbers, electronics, and magnetic storage devices [1, 2].

The structure of ferrite may be tailored, although fundamental configuration continues to exist identical.

Nanocrystalline magnetic materials can be obtained by different methods such as co-precipitation [1, 3–6], hydrothermal [7], sonochemical [8], citrate precursor [9], and sol–gel auto combustion [10–12]. Our present study is on soft ferrites which have many applications such as microwave devices, thermo-junctions, high-frequency cores, humidity sensors, antennas, multilayer chip inductor (MLCI), high-frequency transformers, ferrite wave absorber, electronics, and magnetic storage devices [13].

The physical properties of ferrites are powerfully dependent on many parameters, like particle size, crystallite dimensions, and cationic distribution, and their purity is extensively interrelated with the method of synthesis of the ferrites [14].

Ferrites display interesting and fruitful variations in electrical properties by the inclusion of various cations within ferrite materials [15]. Structural and electrical characteristics of ferrites were upgraded by many researchers by the inclusion of rare-earth ions [16–19].

In our present study, Ce-Cd system was synthesized, with general formula $CdFe_{2-x}Ce_xO_4$, where $0 \le x \le 0.5$ (Ce^{3+}-doped CF). The rare earth metal cerium was doped in the cadmium soft ferrites which have a normal spinel structure. Five samples were prepared with compositions $x = 0.0$, 0.125, 0.25, 0.375, and 0.5 by chemical co-precipitation approach to observe their electrical, dielectric and structural characteristics. The content of rare earth metal cerium was increased in regular steps, and the nanoparticles were fabricated for the said compositions. At last, the prepared samples were characterized using XRD, FTIR, LCR, and I-V.

2 Materials and Method

To prepare $CdFe_{2-x}Ce_xO_4$, metal solutions of required molarities were prepared by dissolving cadmium nitrate, cerium chloride, and iron chloride in deionized water. Cerium-doped cadmium ferrites $CdFe_{2-x}Ce_xO_4$ were synthesized by using the highly pure cadmium nitrate tetrahydrate $Cd(NO_3)_2{\cdot}4H_2O$, ferric chloride hexahydrate $FeCl_3{\cdot}6H_2O$, and cerium chloride heptahydrate $CeCl_3{\cdot}7H_2O$. Five samples were prepared with the composition $x = 0.0$, 0.125, 0.25, 0.375, and 0.5. There are several methods to dope cerium into cadmium soft ferrites, but the chemical co-precipitation method was used in this study. Materials were measured according to the stoichiometry calculation. The measured quantities of these materials were mixed and dissolved into 100 ml of de-ionized water in the beakers separately. These solutions of the samples were stirred on the stirrer, and a solution of NaOH was poured dropwise into the solution until the pH of the solution became 11 and the stirring process was stopped. After this solution was put into a water bath maintained at a temperature of 80 °C for 24 h. The pH of the solution was made 7 by washing precipitates with deionized water. The substance that was left after washing was dried in an oven for 36 h. After that, each sample was ground in a pestle and mortar for 1 h to make it in powder form. After grinding, samples were placed in a furnace for sintering at 900 °C for 8 h. The purpose of sintering is to compact the material. After sintering the substance was ground further for 1 h in the pestle and mortar to make it powder. This powder was characterized using XRD, I-V, LCR, and FTIR.

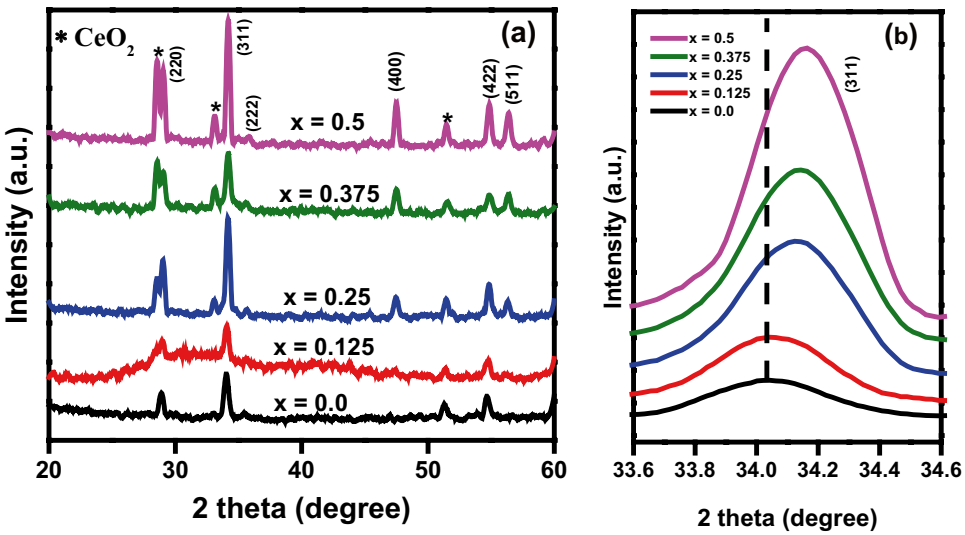

Fig. 1 (**a**) XRD patterns for Ce^{3+}-doped CF samples. (**b**) Peaks (311) shift towards right

Table 1 Crystallite size, lattice constant, unit cell volume, and X-ray density for (220), (311), and (511) plans of the as-prepared samples

Samples	Miller indices (*hkl*)											
	(220)	(311)	(511)	(220)	(311)	(511)	(220)	(311)	(511)	(220)	(311)	(511)
	Crystallite size D (nm)			Lattice parameter a (Å)			Unit cell volume V_{cell} (Å^3)			X-ray density d_X(g/cm^3)		
$CdFe_2O_4$	27	28	24	8.7336	8.7293	8.7254	665.98	664.43	665.56	5.75	5.76	5.75
$CdFe_{1.875}Ce_{0.125}O_4$	29	32	32	8.7156	8.7041	8.7016	664.60	662.00	661.44	5.97	5.99	5.99
$CdFe_{1.75}Ce_{0.25}O_4$	33	33	34	8.7048	8.6891	8.6956	657.80	658.54	660.08	6.24	6.24	6.22
$CdFe_{1.625}Ce_{0.375}O_4$	36	35	37	8.6948	8.6841	8.6719	657.80	657.43	654.70	6.46	6.46	6.49
$CdFe_{1.5}Ce_{0.5}O_4$	48	46	47	8.6909	8.6891	8.6926	657.80	658.57	659.41	6.67	6.67	6.65

3 Results and Their Discussion

3.1 Structural Analysis

The XRD patterns of Ce^{3+}-doped CF samples are shown in Fig. 1a. The diffraction peaks were labeled with planes (220), (311), (222), (400), (422), and (511), and well-matched with the standard JCPDS Card Nos. 00–086-2267 and 00–08-0234, also confirmed the formation of cubic spinel Ce^{3+}-doped CF ferrites. [20]. The additional peaks of CeO_2 [21, 22] well-matched with JCPDS card No. 81–0792 represented by a symbol (*), as shown in Fig. 1a. Secondary phases of cerium oxide CeO_2 appeared when cerium concentration was enhanced from $x=0$ and intensity of peak continues to increase with the rise of cerium concentration which may be due to (a) less solubility of cerium contrary to that of iron and (b) greater bond energy of $Ce^{3+\overline{\ }}O^2$ as compared to $Fe^{3+\overline{\ }}O^{2-}$. Hence, the immense amount of energy is needed to incorporate Ce^{3+} ions for Fe^{3+} ions, and this creates secondary phases [23, 24]. It was also observed from Fig. 1b that the peak with the plane (311) shifts toward a greater angle and the intensity of peaks decreases as increasing Ce^{3+} cations, which may be due to oxygen vacancies and strain production [21].

The prominent peaks (220), (311), and (511) were used to determine the crystallite size (D) of the as-prepared ferrites using Scherrer's relation [25];

$$D = \frac{0.9\lambda}{\beta \cos \theta} \tag{1}$$

where 0.9 is Scherrer constant. β, λ, and θ represent full width at half maximum height of diffraction peak, the wavelength of the X-ray used, and Bragg's angle, respectively. The crystallite size (D) was increased with Ce^{3+} doping for the (220), (311), and (511) peaks (Table 1) and graphically represented in Fig. 2a. The lattice constant (a), unit cell volume $\left(V_{\text{cell}}\right)$, and X-ray density $\left(d_X\right)$ were determined using relation (2), (3), and (4), respectively [26, 27] and reported in Table 1.

$$a = \frac{\lambda}{2 \sin \theta}\sqrt{h^2 + k^2 + l^2} \tag{2}$$

where λ indicates the wavelength of the X-ray beam used and "θ" stands for Bragg's angle. (*hkl*) are the corresponding miller indices to each peak in the pattern [28, 29].

$$V_{\text{cell}} = a^3 \tag{3}$$

$$d_X = \frac{ZM_w}{V_{\text{cell}}N_A} \tag{4}$$

where $Z=8$ indicates the number of formula units present in a unit cell for spinel ferrite. M_w represents the molecular

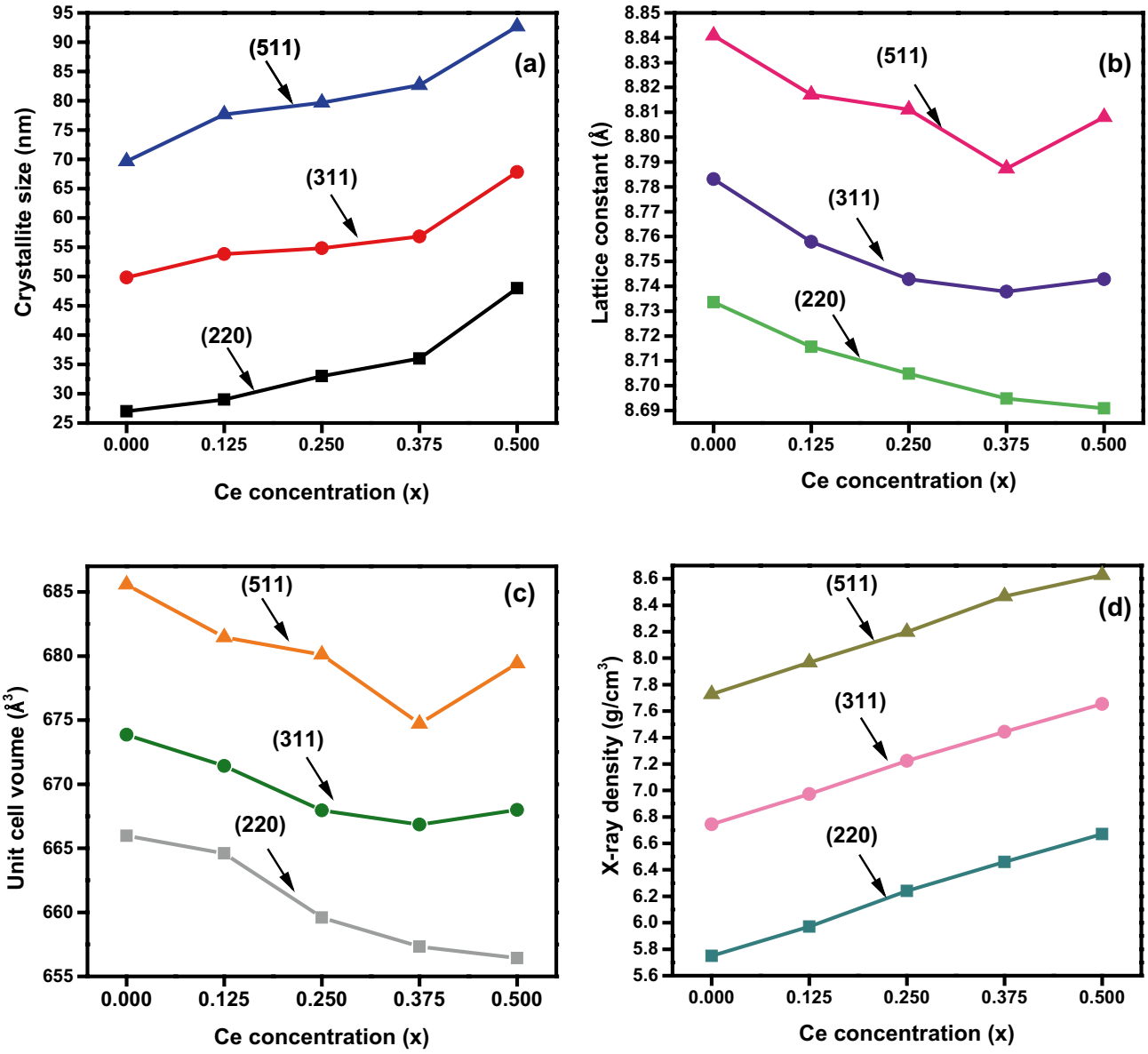

Fig. 2 Plots of Ce concentration (x) *versus* (**a**) crystallite size, (**b**) lattice constant, (**c**) unit cell volume, and (**d**) X-ray density for (220), (311), and (511) planes

weight of synthesized nano ferrites and N_A is Avogadro's number. The graphical representation of Ce^{3+} concentration (x) *versus* lattice constant (a), unit cell volume (V_{cell}), and X-ray density (d_X) for the (220), (311), and (511) peaks are depicted in Fig. 2b–d. The change in the lattice parameters may be due to the insertion of a large ionic radius of Ce^{3+} (1.143 Å) as compared to Fe^{3+} (0.645 Å) [30].

Cd^{2+} is a divalent metal ion, whereas Ce^{3+} has a trivalent metal ion, in which Cd^{2+} occupies the tetrahedral site and both Ce^{+3} and Fe^{+3} occupy the octahedral site. Hence, cation distribution for Ce^{3+}-doped CF samples is reported in Table 2. The radii at the tetrahedral (A) and octahedral (B) sites were calculated using the following relation:

$$r_A = \left[C_{\text{Cd}} r\left(\text{Cd}^{2+}\right)\right] \tag{5}$$

$$r_B = \frac{1}{2}\left[C_{\text{Ce}} r\left(\text{Ce}^{3+}\right) + C_{\text{Fe}} r\left(\text{Fe}^{3+}\right)\right] \tag{6}$$

The ionic radii: $r\left(\text{Cd}^{2+}\right) = 0.78\text{A}°$, $r\left(\text{Ce}^{3+}\right) = 1.143$ A°, $r\left(\text{Fe}^{3+}\right) = 0.645$ A° [31]. C_{Cd}, C_{Fe}, and C_{Ce} represent the concentration of Cd^{2+}, Ce^{3+}, and Fe^{3+} ions on different sites. The result is summarized in Table 2. The theoretical lattice constant (a_{th}) was calculated by Eq. (7) and is given in Table 2.

$$a_{\text{th}=8/3\sqrt{3}[(r_A+r_o)+\sqrt{3}(rB+r_o)]} \tag{7}$$

Table 2 The theoretical value of the lattice parameter (a_{th}), radii of octahedral and tetrahedral (r_A and r_B), oxygen ion parameter (u), hopping lengths (L_A, L_B), bond lengths at A- and B-sites (d_{AL},d_{BL}), shared tetrahedral edge length (d'), and shared and unshared octahedral edge lengths (d'',d''')

Cation distribution	a_{th}(Å)	r_A(Å)	r_B(Å)	u (Å)	L_A(Å)	L_B(Å)	d_{AL}(Å)	d_{BL}(Å)	d'(Å)	d''(Å)	d'''(Å)
(Cd)[Fe_2] O_4	8.47	0.78	0.64	0.3888	3.7799	3.0862	2.1	2.0681	3.429	2.7432	3.0957
(Cd)[$Ce_{0.125}Fe_{1.875}$] O_4	8.55	0.78	0.67	0.3892	3.7689	3.0773	2.1	2.0591	3.429	2.7254	3.0874
(Cd)[$Ce_{0.25}Fe_{1.75}$] O_4	8.63	0.78	0.7	0.3895	3.7624	3.072	2.1	2.0537	3.429	2.7148	3.0824
(Cd)[$Ce_{0.375}Fe_{1.625}$] O_4	8.72	0.78	0.73	0.3896	3.7603	3.0702	2.1	2.0519	3.429	2.7113	3.0807
(Cd)[$Ce_{0.5}Fe_{1.5}$] O_4	8.80	0.78	0.76	0.3895	3.7624	3.0720	2.1	2.0537	3.429	2.7148	3.0824

where r_o = 1.32 Å represents ionic radii of oxygen. The comparison of the experimental and theoretical lattices constant represented in Fig. 3a. The theoretical value of the lattice constant (a_{th}) was found to increase with the addition of cerium as shown in Fig. 3a. This increasing trend could be associated with the increasing cerium content where the ionic radius of Ce^{3+} (1.143 Å) is larger than that of Fe^{3+} ion (0.645 Å) replacing iron ions on octahedral *B*-site which causes asymmetry in the structure. Hence, the lattice constant should be increased with the increasing content of the Ce^{3+} during the substitution process [23]. Besides this, a decreasing trend was observed in the experimental value of the lattice parameter with the inclusion of dopant ions which could be attributed to the compression of spinel lattice induced by the secondary phases. The secondary phases are formed on the surface of grains during the calcination process. The deformity in the internal grain region due to the induced secondary phases corresponds to the contraction of spinel lattice and as a result, the lattice parameter diminished. The doping ions, calcination temperature, and time are responsible for the contraction of the spinel lattice. Sintering conditions are very important for the diffusion of ions into the spinel lattice [23, 32, 33]. The oxygen ion parameter (u) depends upon chemical composition, preparation condition, and sintering procedure and can be calculated by using Eq. (8);

$$u = \left[(r_A + r_O)1/\sqrt{3}a + 1/4\right] \tag{8}$$

The oxygen ion parameter and lattice parameter increase by increasing Ce doping and are listed in Table 2. The hopping length of *A* site, as well as B-site, were determined by relation:

$$L_A = a\left(\sqrt{3}\right)(\Delta + 1/8) \tag{9}$$

$$L_B = a\left(3\Delta^2 - \frac{\Delta}{2} + 1/16\right) \tag{10}$$

where the smallest space of A-site cation and B-site cation from oxygen ion is represented by L_A and L_B, respectively. $\Delta = (u - 0.375)$ is deviance from the ideal "u" parameter. The hopping length variation *versus* cerium concentration is represented in Fig. 3b. The bond lengths at A- and B-sites (d_{AL},d_{BL}), shared tetrahedral edge length (d), and shared and

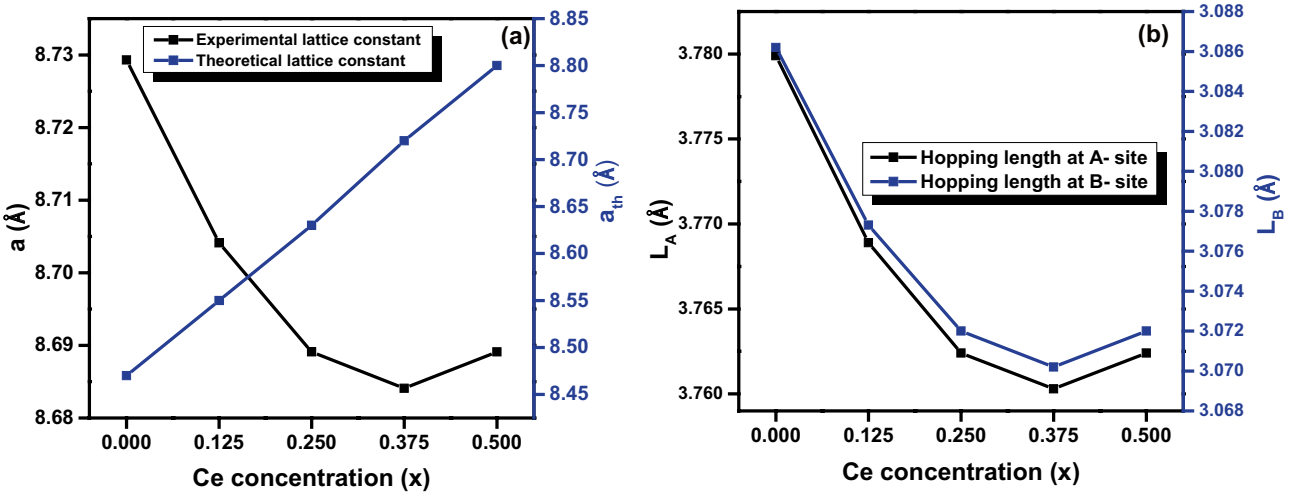

Fig. 3 Plots of (**a**) Ce concentration (x) *versus* experimental and theoretical lattice constants and (**b**) Ce concentration (x) *versus* hopping length at A- and B-sites

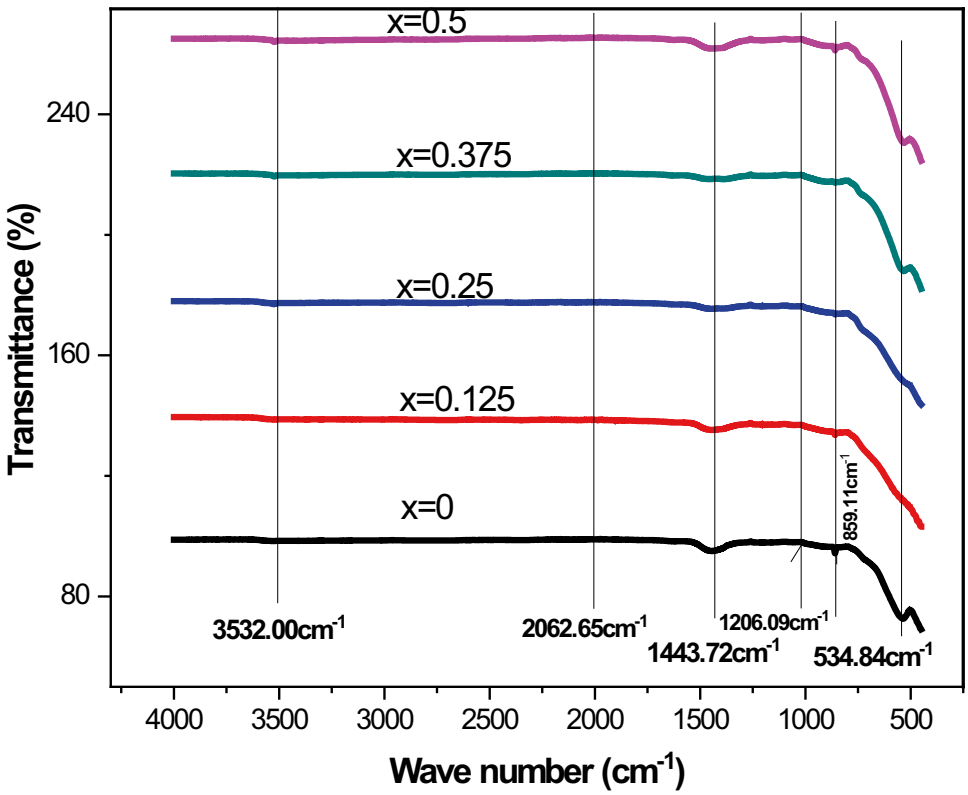

Fig. 4 FTIR spectra of the Ce^{3+}-doped CF samples

unshared octahedral edge lengths (d'', d''') were calculated and are given in Table 2.

3.2 FTIR Analysis

Functional group analysis and absorption bands of Ce^{3+}-doped CF samples were found by performing FTIR analysis. Two main absorption bands are observed in the range of 1000 to 400 cm^{-1} as clear from Fig. 4. The absorption band around ~ 534 cm^{-1} corresponds to the tetrahedral vibrations, and ~ 416 cm^{-1} corresponds to the octahedral vibrations. These bands may be due to stretching vibrations of metal and oxygen ions at tetrahedral and octahedral sites. From the FTIR spectra, band is shifted to the lower wavelength which may be attributed to the increase of Ce^{3+} ions in the ferrite. The Cd^{2+} ions preferably occupy the tetrahedral (*A*) site in the spinel ferrites [31]. The absorption band around ~ 3532 cm^{-1} corresponds to the O–H peak and indicates the presence of adsorbed water [34]. The peaks around ~ 2062 cm^{-1} are attributed to the C ≡ N stretching. Bands around 1443 cm^{-1} and 859.11 cm^{-1} correspond to the C-N stretching. The absorption band around 1206 cm^{-1} corresponds to the C-F stretching.

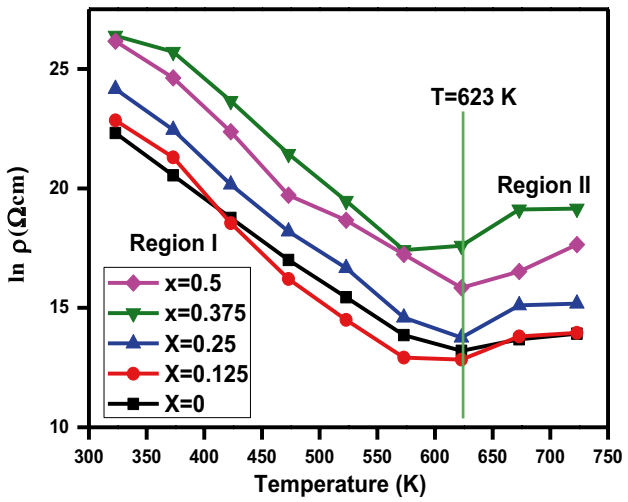

Fig. 5 Plot of temperature *versus* variation of ln ρ of $CdFe_{2-x}Ce_xO_4$

Table 3 Electrical resistivity of $CdFe_{2-x}Ce_xO_4$ at different temperatures

Composition	Resistivity × 10^8 (Ω cm)				
	313 K	423 K	523 K	623 K	723 K
$CdFe_2O_4$	63.21	1.40	0.074	0.0054	0.011
$CdFe_{1.875}Ce_{0.125}O_4$	42.00	0.42	0.013	0.0013	0.0042
$CdFe_{1.75}Ce_{0.25}O_4$	59.068	0.77	0.032	0.0013	0.0053
$CdFe_{1.625}Ce_{0.375}O_4$	121.49	9.40	0.213	0.0219	0.1030
$CdFe_{1.5}Ce_{0.5}O_4$	44.05	0.95	0.035	0.0014	0.0085

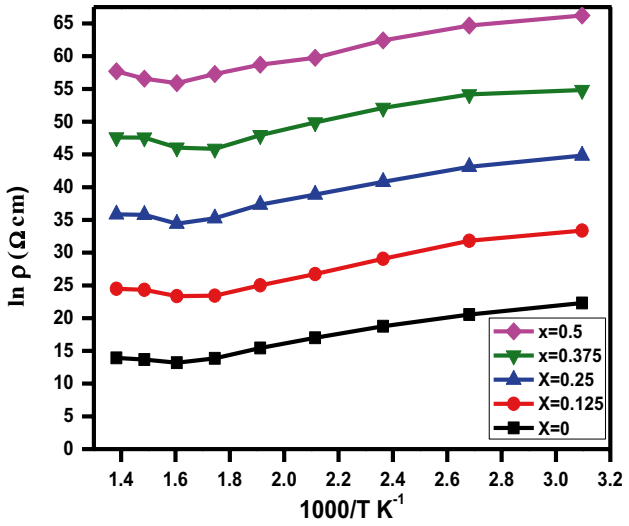

Fig. 6 Plot of 1000/T *versus* ln ρ

3.3 I-V Measurement Analysis

The electrical resistivity of Ce^{3+}-doped CF samples sintered at 900 °C were computed employing two probes approach in a temperature span of 40–450 °C. Resistances of manufactured samples were evaluated using the slope of the I-V graph, where the voltage was along the *x*-axis and current was plotted along the *y*-axis. The formula is as follows;

$$R = \frac{1}{\text{slope}} \tag{11}$$

The electrical resistivity of manufactured samples was determined using the mathematical expression;

$$\rho = \frac{RA}{h} \tag{12}$$

where "*h*" represents the thickness of pallets. "*A*" gives the area of cross-section of pellets prepared from all the samples.

Figure 5 reveals the way electrical resistivity changes with the enhancement of temperature of all the samples of cerium-doped cadmium soft ferrites. Values of resistivity found for different concentrations of cerium-doped cadmium ferrites at certain temperatures 313 K, 423 K, 523 K, 673 K, and 723 K are given in Table 3. Table 3 reveals that the resistivity of pure $CdFe_2O_4$ at 313 K (room temperature) is very high (63.21×10^8 Ω cm) and its value decreases with the increasing temperature up to 623 K (63.21×10^8 to 0.0054×10^8 Ω cm) and increases when the temperature is further increased from 623 K (0.011×10^8 Ω cm). The same trend is seen for all the samples as is clear from Fig. 5. Change in behavior of resistivity indicates that the nature of magnetic materials changes from one form to another [35]. Region-I has the ferromagnetic nature of the samples as Fig. 5 declares a decrease in resistivity with the rise of temperature and region-II indicates the paramagnetic nature of the materials. To evaluate the activation energy of the samples, Arrhenius plots are drawn (Fig. 6). The conduction mechanism in ferrites is the hopping mechanism. According to the hopping mechanism, when the temperature of ferrites increases, mobility of charge carriers also increases, and a

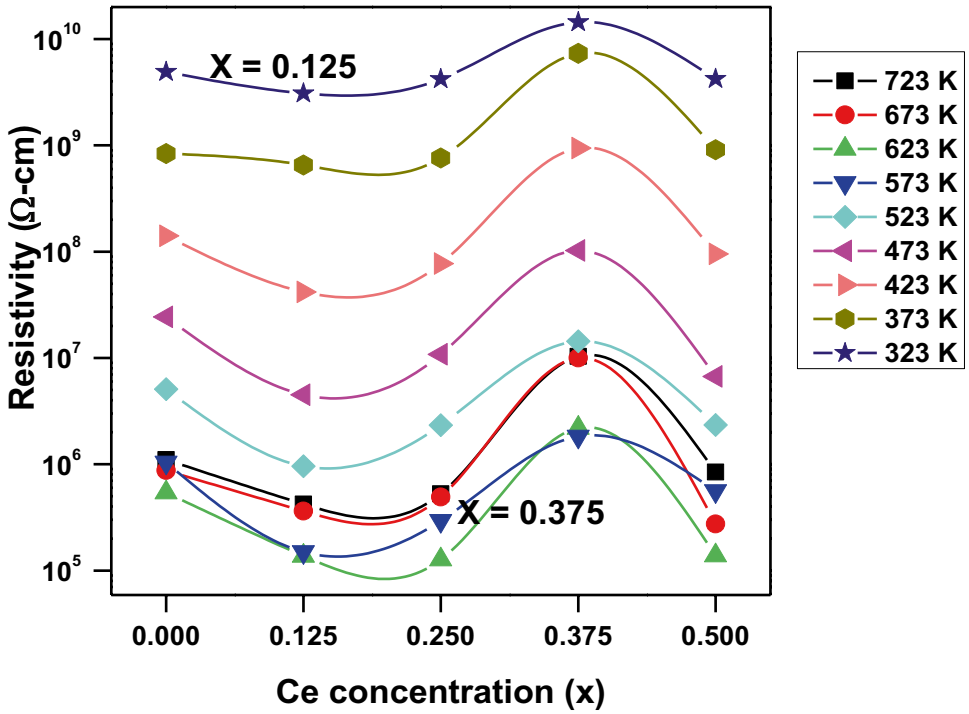

Fig. 7 Plot of Ce concentration *versus* resistivity

Table 4 Drift mobility, carrier concentration, and activation energy at 673 K

Parameters	$x=0.0$	$x=0.125$	$x=0.25$	$x=0.375$	$x=0.5$
$\mu_d \times 10^{-10}$ **at 673 K**	5.68	6.21	12.16	6.70	27.74
$\eta \times 10^{22}$	1.258	1.149	1.046	0.934	0.821
E_I(eV)	1.2356	1.5109	1.3903	1.3403	1.3647
E_{II}(eV)	− 0.0642	− 1.0211	− 1.2986	− 1.4164	− 1.6069
$\Delta E = E_I - E_{II}$(eV)	1.8784	2.5320	2.6943	2.7568	2.9716

current flow by hopping from one iron atom to the other. So, ferrite conduction is imputed to the mechanism of hopping of electrons between ferrous (Fe^{2+}) and ferric (Fe^{3+}) at octahedral sites. The resistivity of samples with composition has random behavior as is clear from Fig. 7, but the resistivity at $x=0.125$ has a minimum value and at $x=0.375$ has a maximum value at almost all temperatures as shown in Table 3. Figure 7 exhibits that the resistivity increased for all the samples except for the samples with concentrations $x=0.125$ and $x=0.5$. This increase in resistivity may be due to the insertion of cerium (75 μΩ cm) at the place of iron (9.71 μΩ cm) [36]. The decrease in the value of resistivity at $x=0.5$ may be attributed to the secondary phase (CeO_2) that reside at the grain boundaries and hinder the further migration of iron (Fe^{3+}) from octahedral site to tetrahedral site, so hopping of electrons between Fe^{3+} and Fe^{2+} increases resulting in a decrease in resistivity [37]. Figure 6 shows graphs of ln ρ *vs.* 1000/T for Ce^{3+}-doped CF samples. Activation energies (E_a) were determined employing formula [35, 36].

$$E_a = 2.303 \times K_B \times 10^3 \times \text{slope(eV)} \tag{13}$$

where the value of Boltzmann constant $k_B = 8.602 \times 10^{-5}$ eV/K. Table 4 shows that the activation energy of fabricated nano-ferrites increased with an increase of dopant concentration and also as cleared from Fig. 8, Same results reported in papers [36].

The drift mobility (μ_d) for fabricated samples was evaluated using equation [38, 39];

$$\mu_d = \frac{1}{\eta e \rho} \tag{14}$$

where "e" represents the charge on the electron, "ρ" shows DC electrical resistivity, and "η" is charge carriers concentration. The following relation was employed for the evaluation of η is [40, 41];

$$\eta = \frac{N_a \rho_s P_{\text{Fe}}}{M} \tag{15}$$

where "M" represents molecular weight. "Na" shows Avogadro's number. Sintered density is represented by "ρ_s," and the number of iron atoms in the chemical formula of ferrite is represented by "P_{Fe}." Fig. 9 helps to comprehend the relationship between drift mobility and temperature. From the plot (Fig. 9), drift mobility rises with the enhancement of temperature till 623 K and after that drift mobility starts

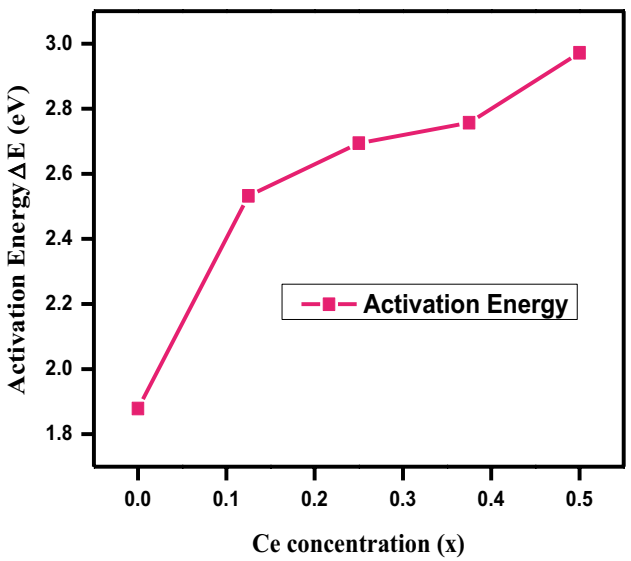

Fig. 8 Plot of activation energy as a function of composition

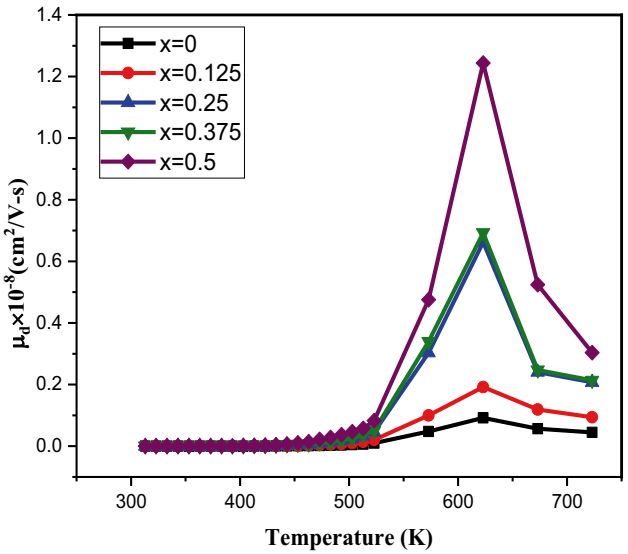

Fig. 9 Plot of drift mobility of $CdFe_{2-x}Ce_xO_4$ ($x=0$, 0.125, 0.25, 0.375, and 0.50) with temperature

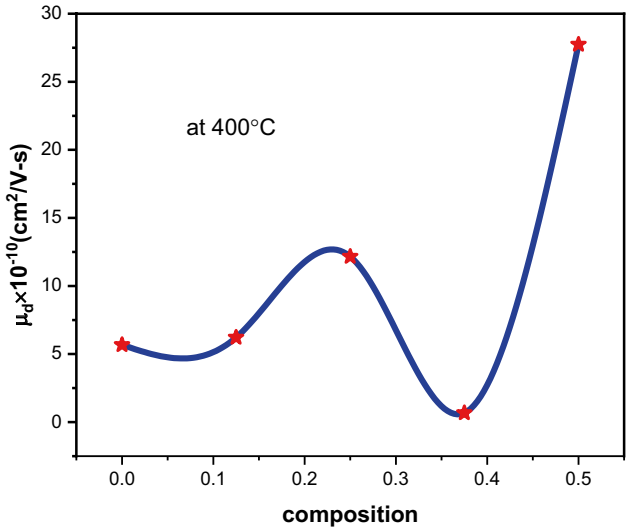

Fig. 10 Plot of Cerium concentration vs drift mobility of $CdFe_{2-x}Ce_xO_4$ ($x=0$, 0.125, 0.25, 0.375 and 0.50) at 673 K

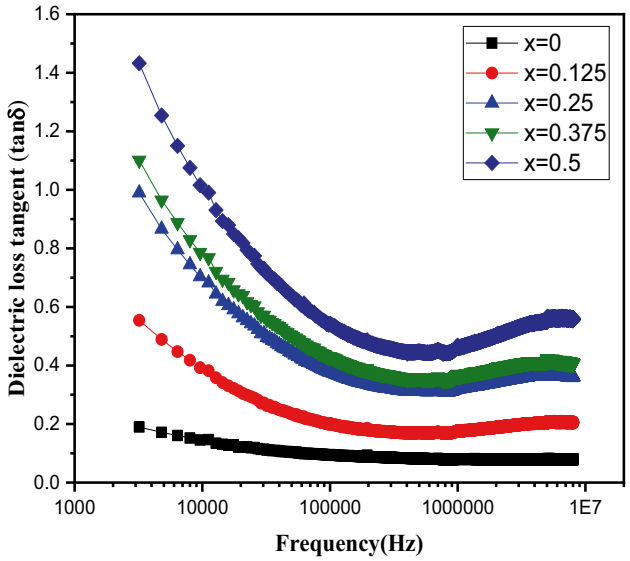

Fig. 12 Plot of dielectric loss tangent of $CdFe_{2-x}Ce_xO_4$ ($x=0$, 0.125, 0.25, 0.375, and 0.50) vs frequency

to reduce with a rise in temperature and resistivity increases correspondingly. This shows that the change in mobility with temperature is responsible for the disparity of resistivity with the temperature rise. Hence, with the enhancement of temperature, charge carriers begin to hop from one site to another increasing the drift mobility and decreasing the resistivity of Nano ferrites. The values of carrier concentration and drift mobility are given in Table 4. It was seen from Fig. 10 that drift mobility increased from 5.68×10^{-10} to 27.74×10^{-10} cm^2/Vs at 673 K for the concentration of cerium from $x=0$ to $x=0.50$ except $x=0.375$.

3.4 Dielectric Properties

The graph of dielectric constant versus frequency for all the samples at ambient temperature is shown in Fig. 11 which shows a reducing trend of dielectric constant with the rise in frequency. This exhibits that cerium-doped cadmium ferrites depict normal dielectric behavior. Many researchers found the same dielectric behavior in many ferrites [36, 40]. When the frequency of applied field increases, then the number of electrons that accumulate at grain boundary decrease and hence interchange of electrons also decreases as a result

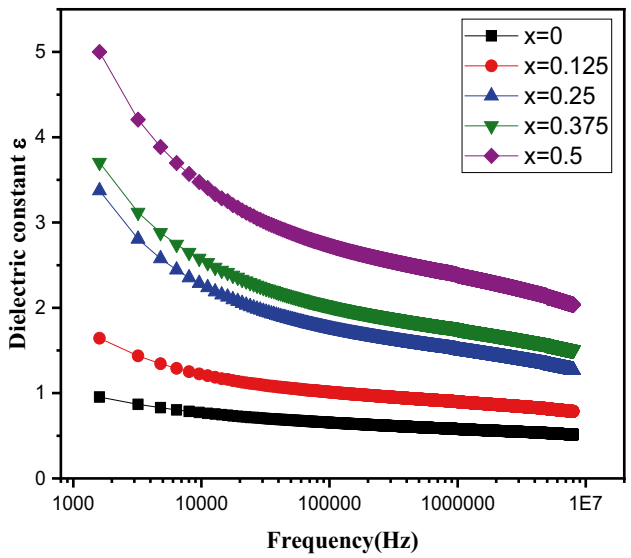

Fig. 11 Plot of the dielectric constant of $CdFe_{2-x}Ce_xO_4$ ($x=0$, 0.125, 0.25, 0.375, and 0.50) vs frequency

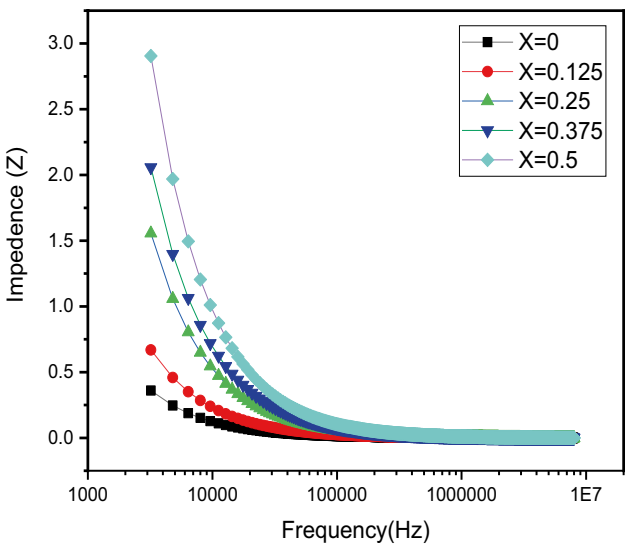

Fig. 13 Plot of the impedance of $CdFe_{2-x}Ce_xO_4$ ($x=0$, 0.125, 0.25, 0.375 and 0.50) vs frequency

polarization decrease and dielectric constant decreases. Figure 12 shows a graph of dielectric loss tangent vs frequency at ambient temperature for all the samples. Dielectric loss reduces with the enhancement of frequency. Figure 13 shows the graph between impedance vs frequency. The impedance has an inverse relation with frequency. The decreasing trend of dielectric constant with an increase in frequency can be interpreted on account of the Maxwell–Wagner model [42, 43]. This model explains that grain boundary having greater resistance separates the conducting grains in every ferrite structure. At low frequency, the values of the dielectric constant are very large due to the presence of polarization which may be due to the accumulation of a large number of electrons on the grain boundary in nanomaterial ferrites. The polarization in ferrites is due to a mechanism same as that of the conduction process. The polarization occurs due to the local displacement of electrons in the direction of the applied field which may be attributed to the interchange of electrons between Fe^{2+} and Fe^{3+} ions on the octahedral site [44].

4 Conclusion

The co-precipitation method was employed for the fabrication of $CdFe_{2-x}Ce_xO_4$ nano ferrite powders. X-ray diffraction study shows cubic spinel ferrites with traces of secondary phases of CeO_2 for all samples with cerium composition. The crystallite size of the synthesized material fluctuates from 28 to 46 nm. FTIR study confirmed metal oxide bands at (531.23–534.84 cm^{-1}) corresponding to the tetrahedral bond vibrations, verifying the formation of the cubic spinel structure of $CdFe_{2-x}Ce_xO_4$. The resistivity of synthesized material was found to reduce with the enhancement of temperature, declaring semiconducting behavior of synthesized Ce-Cd samples. The activation energy increased with an increase in concentration for samples.

Funding The current research is supported by Taif University Researchers Supporting Project number (TURSP—2020/293), Taif University, Taif, Saudi Arabia. The authors extend their appreciation to the Deanship of Scientific Research (DRS), king Khalid University, Abha, Saudi Aribia for funding this work through General Reseach Project, under grant no.G.R.P. 30/42. Khalid Husain also received support from the HEC, Pakistan, through IRSIP, PIN: IRSIP 46 PSc.45.

References

1. Patange, S., Shirsath, S.E., Toksha, B., Jadhav, S.S., Jadhav, K.: Electrical and magnetic properties of Cr^{3+} substituted nanocrystalline nickel ferrite, J. Appl. Phys. **106**, 023914 (2009)
2. Nejati, K., Zabihi, R.: Preparation and magnetic properties of nano size nickel ferrite particles using hydrothermal method. Chem. Cent. J. **6**, 1–6 (2012)
3. ALIa, I., Amin, N., Rehman, A., Akhtar, M., Fatima, M., Mahmood, K., ALIa, A., Mustafa, G., Hasan, M.S., Bibi, A.: Electrical and magnetic properties of $BaCo_xCd_{2x}Fe_{16}O_{27}$ W-type hexaferrites ($0 \leq x \leq 0.5$). Digest J. Nanomater. Biostruct. **15**, (2020)
4. Amin, N., Akhtar, M., Sabir, M., Mahmood, K., ALIa, A., Mustafa, G., Hasan, M.S., Bibi, A., Iqbal, M.Z., Iqbal, F.: Synthesis, structural and optical properties of Zn-substituted Co W-ferrites by coprecipitation method. J. Ovonic Res. **16**, 11–19 (2020)
5. Amin, N., Hasan, M.S.U., Majeed, Z., Latif, Z., un Nabi, M.A., Mahmood, K., Ali, A., Mehmood, K., Fatima, M., Akhtar, M.: Structural, electrical, optical and dielectric properties of yttrium substituted cadmium ferrites prepared by Co-Precipitation method. Ceram. Int. **46**, 20798–20809 (2020)
6. Aslam, A., Rehman, A.U., Amin, N., un Nabi, M.A., ul ain Abdullah, Q., Morley, N.A., Arshad, M.I., Ali, H.T., Yusuf, M., Latif, Z.: Lanthanum doped $Zn_{0.5}Co_{0.5}La_xFe_{2-x}O_4$ spinel ferrites synthesized via co-precipitation route to evaluate structural, vibrational, electrical, optical, dielectric, and thermoelectric properties. J. Phys. Chem. Solids. **154**, 110080 (2021)
7. Nejati, K., Zabihi, R.: Preparation and magnetic properties of nano size nickel ferrite particles using hydrothermal method. Chem. Cent. J. **6**, 23 (2012)
8. Goswami, P.P., Choudhury, H.A., Chakma, S., Moholkar, V.S.: Sonochemical synthesis and characterization of manganese ferrite nanoparticles. Ind. Eng. Chem. Res. **52**, 17848–17855 (2013)
9. Atassi, Y., Tally, M.: Low sintering temperature of Mg-Cu-Zn ferrite prepared by the citrate precursor method. J. Iran. Chem. Soc. **3**, 242–246 (2006)
10. Shirsath, S.E., Kadam, R., Gaikwad, A.S., Ghasemi, A., Morisako, A.: Effect of sintering temperature and the particle size on the structural and magnetic properties of nanocrystalline $Li_{0.5}Fe_{2.5}O_4$. J. Magnet. Magnet. Mater. **323**, 3104–3108 (2011)
11. Rehman, A.U., Morley, N.A., Amin, N., Arshad, M.I., un Nabi, M.A., Mahmood, K., Ali, A., Aslam, A., Bibi, A., Iqbal, M.Z.: Controllable synthesis of La^{3+} doped $Zn_{0.5}Co_{0.25}Cu_{0.25}Fe_{2-x}La_xO_4$ (x = 0.0, 0.0125, 0.025, 0.0375, 0.05) nano-ferrites by sol-gel auto-combustion route. Ceram. Int. **46**, 29297–29308 (2020)
12. Aslam, A., Morley, N.A., Amin, N., Arshad, M.I., un Nabi, M.A., Ali, A., Mahmood, K., Bibi, A., Iqbal, F., Hussain, S.: Study of structural, optical and electrical properties of La^{3+} doped $Mg_{0.25}Ni_{0.15}Cu_{0.25}Co_{0.35}Fe_{2-x}La_xO_4$ spinel ferrites. Phys. B: Condens. Matter. **602**, 412565 (2021)
13. Karanjkar, M., Tarwal, N., Vaigankar, A., Patil, P.: Structural, Mössbauer and electrical properties of nickel cadmium ferrites. Ceram. Int. **39**, 1757–1764 (2013)
14. Zamani, F., Taghvaei A.H.: Synthesis of nanocrystalline $Mg_{0.6}Cd_{0.4}Fe_2O_4$ ferrite by glycine-nitrate auto-combustion method and investigation of its microstructure and magnetic properties. Ceram. Int. **43**, 16693–16702 (2017)
15. Kumar, S., Kumar, R., Sharma, S., Reddy, V., Banerjee, A.: Temperature-dependent Mössbauer and dielectric studies of $Mg_{0.95}Mn_{0.05}Fe_{1.0}Ti_{1.0}O_4$. Solid State Commun. **142**, 706–709 (2007)
16. Sharma, R., Singhal, S.: Structural, magnetic and electrical properties of zinc doped nickel ferrite and their application in photo catalytic degradation of methylene blue. Phys. B **414**, 83–90 (2013)
17. Akhtar, M.N., Sulong, A., Akhtar, M., Khan, M.A.: Systematic study of Ce^{3+} on the structural and magnetic properties of Cu nanosized ferrites for potential applications. J. Rare Earths **36**, 156–164 (2018)

18. Lohar, K., Patange, S., Mane, M., Shirsath, S.E.: Cation distribution investigation and characterizations of $Ni_{1-x}Cd_xFe_2O_4$ nanoparticles synthesized by citrate gel process. J. Mol. Struct. **1032**, 105–110 (2013)
19. Ali, H.T., Ramzan, M., Arshad, M.I., Morley, N.A., Abbas, M.H., Yusuf, M., Rehman, A.U., Mahmood, K., Ali, A., Amin, N.: Tailoring the optical, and magnetic properties of La-BaM hexaferrites by Ni substitution. Chin. Phys. B (2021). https://doi.org/10.1088/1674-1056/ac1412
20. Mustafa, G., Islam, M.U., Zhang, W., Jamil, Y., Iqbal, M.A., Hussain, M., Ahmad, M.: Temperature dependent structural and magnetic properties of Cerium substituted Co–Cr ferrite prepared by auto-combustion method, Journal of Magnetism and Magnetic Materials, **378**, 409–416 (2015)
21. Akhtar, M.N., Khan, M.A.: Effect of rare earth doping on the structural and magnetic features of nanocrystalline spinel ferrites prepared via sol gel route. J. Magn. Magn. Mater. **460**, 268–277 (2018)
22. Vasanthi, V., Shanmugavani, A., Sanjeeviraja, C., KalaiSelvan, R.: Microwave assisted combustion synthesis of $CdFe_2O_4$: magnetic and electrical properties. J. Magn. Magn. Mater. **324**, 2100–2107 (2012)
23. Dasan, Y., Guan, B., Zahari, M., Chuan, L.: Influence of La^{3+} substitution on structure, morphology and magnetic properties of nanocrystalline Ni-Zn ferrite. PloS One. **12**, e0170075 (2017)
24. Thakur, P., Sharma, R., Kumar, M., Katyal, S.C., Negi, N.S., Thakur, N., Sharma, V., Sharma, P.: Superparamagnetic La doped Mn–Zn nano ferrites: dependence on dopant content and crystallite size. Mater. Res. Express. **3**, 075001 (2016)
25. Aslam, A., Razzaq, A., Naz, S., Amin, N., Arshad, M.I., Nabi, M.A.U., Nawaz, A., Mahmood, K., Bibi, A., Iqbal, F.: Impact of lanthanum-doping on the physical and electrical properties of cobalt ferrites. J. Supercond. Novel Magnet. 1–10 (2021)
26. Miao, F., Deng, Z., Lv, X., Gu, G., Wan, S., Fang, X., Zhang, Q., Yin, S.: Fundamental properties of $CdFe_2O_4$ semiconductor thin film. Solid State Commun. **150**, 2036–2039 (2010)
27. Iqbal, M.J., Ahmad, Z., Melikhov, Y., Nlebedim, I.C.: Effect of Cu–Cr co-substitution on magnetic properties of nanocrystalline magnesium ferrite. J. Magn. Magn. Mater. **324**, 1088–1094 (2012)
28. JavedIqbal, M., ZahoorAhmad, Y., Melikhov, I.C.: Nlebedim, Effect of Cu–Cr co-substitution on magnetic properties of nano crystalline magnesium ferrite. J. Magn. Magn. Mater. **324**, 1088–1094 (2012)
29. Zakir, R., Iqbal, S.S., Rehman, A.U., Nosheen, S., Ahmad, T.S., Ehsan, N., Inam, F.: Spectral, electrical, and dielectric characterization of Ce-doped Co-Mg-Cd spinel nano-ferrites synthesized by the sol-gel auto combustion method, (2021). https://doi.org/10.1016/j.ceramint.2021.07.016
30. Hussain, K., Amin, N., Ajaz-Un-Nabi, M., Ali, A., Mahmood, K., Mustafa, G., sharif, M., Hassan, M.S., Sabir, N., Ali, S., Jabeen, F., Asif, M., Arshad, M.I.: Investigation of structural and electrical properties of Ce^{3+} ions substituted Cd-Co ferrites. Digest J. Nanomater. Biostruct. **14**, 85–92 (2019)
31. Belavia, P.B., Chavana, G.N., Naika, L.R., Somashekarb, R., Kotnala, R.K.: Structural, electrical and magnetic properties of cadmium substituted nickel–copper ferrites. Mater. Chem. Phys. **132**, 138– 144 (2012)
32. Al-Hilli, M.F., Li, S., Kassim, K.S.: Microstructure, electrical properties and Hall coefficient of europium-doped Li–Ni ferrites. Mater. Sci. Eng., B **158**, 1–6 (2009)
33. Manzoor, A., Khan, M.A., Khan, M.Y., Akhtar, M.N., Hussain, A.: Tuning magnetic and high frequency dielectric behavior in Li-Zn ferrites by Ho doping. Ceram. Int. **44**, 6321–6329 (2018)
34. Padalia, D., Johri, U.C., Zaidi, M.G.H.: Study of cerium doped magnetite (Fe_3O_4:Ce)/PMMA nano composites. Phys. B **407**, 838–843 (2012)
35. Raghasudha, M., Ravinder, D., Veerasomaiah, P.: Electrical resistivity studies of Cr doped Mg nano-ferrites, Materials. Discovery **2**, 50–54 (2015)
36. Malana, M.A., Qureshi, R.B., Ashiq, M.N., Zafar, Z.I.: Synthesis, electrical and dielectric characterization of cerium doped nano copper ferrites. Mater. Res. Bull. **48**, 4775–4779 (2013)
37. Yousuf, M.A., Jabeen, S., Shahi, M.N., Khan, M.A., Shakir, I., Warsi, M.F.: Magnetic and electrical properties of yttrium substituted manganese ferrite nanoparticles prepared via micro-emulsion route. Results Phys. **16**, 102973 (2020)
38. Naeem, M., Shah, N.A., Gul, I.H., Maqsood, A.: Structural, electrical and magnetic characterization of Ni–Mg spinel ferrites. J. Alloy. Compd. **487**, 739–743 (2009)
39. Hussain, K., Amin, N., Arshad, M.I.: Evaluation of structural, optical, dielectric, electrical, and magnetic properties of Ce^{3+} doped $Cu_{0.5}Cd_{0.25}Co_{0.25}Fe_{2-x}O_4$ spinel nano-ferrites. Ceram. Int. **47**, 3401–3410 (2021)
40. Gul, I., Ahmed, W., Maqsood, A.: Electrical and magnetic characterization of nanocrystalline Ni–Zn ferrite synthesis by co-precipitation route. J. Magn. Magn. Mater. **320**, 270–275 (2008)
41. Hussain, K., Bibi, A., Jabeen, F., Amin, N., Mahmood, K., Ali, A., Iqbal, M.Z., Arshad, M.: Study of structural, optical, electrical and magnetic properties of Cu^{2+} doped $Zn_{0.4}Co_{0.6x}Ce_{0.1}Fe_{1.9}O_4$ spinel ferrites. Phys. B: Condens. Matter. **584**, 412078 (2020)
42. Wagner, K.W.: Zur theorie der unvollkommenen dielektrika. Ann. Phys. **345**, 817–855 (1913)
43. Maxwell, J.C.: Electricity and magnetism, Dover New York (1954)
44. Fawzi, A.S., Sheikh, A., Mathe, V.: Structural, dielectric properties and AC conductivity of Ni(1–x)ZnxFe2O4 spinel ferrites. J. Alloy. Compd. **502**, 231–237 (2010)